Journal of Materials Chemistry A

ROYAL SOCIETY OF CHEMISTRY

PAPER

View Article Online
View Journal | View Issue

Check for updates

Cite this: J. Mater. Chem. A, 2025, 13, 9252

Phenothiazine-based self-assembled monolayers for efficient tin perovskite solar cells with Co-cations†

Atika Abid,‡[a] Arulmozhi Velusamy,‡[b] Shakil N. Afraj,[b] Waqas Pervez,[c] Ting-Yu Su,[b] Shao-Huan Hong,[d] Cheng-Liang Liu,[d] Ming-Chou Chen *[b] and Eric Wei-Guang Diau *[a]

Received 9th November 2024
Accepted 16th February 2025

DOI: 10.1039/d4ta07975b

rsc.li/materials-a

We developed three self-assembled monolayer (SAM) molecules, **PTz**[2] (**1**), **PTz** (**2**) and **PTzBr** (**3**), and investigated the mixing of guanidinium (GA) and methylammonium (MA) cations at the A-site, alongside formamidinium (FA), to create mixed cations during the deposition of the tin perovskite layer onto phenothiazine-based SAM-coated ITO substrates using a two-step fabrication method. This study reveals the synergy between the larger ammonium-like GA cations and FA, resulting in the structure $FA_{0.75}GA_{0.25}SnI_3$ that inhibits moisture diffusion into the perovskite layer to provide ideal grain passivation. Consequently, the **PTzBr** (**3**) SAM-based device showed the best performance, achieving a power conversion efficiency of 7.8% and showing negligible hysteresis effects. Additionally, the **PTzBr** (**3**) device demonstrated remarkable long-term storage stability, retaining about 80% of its initial efficiency for over 4000 h without encapsulation, and remaining stable for 9 h under one-sun illumination. The thermal, morphological, optical, electrochemical, charge recombination, and single-crystal properties of the phenothiazine-based SAMs (**1**–**3**) were also investigated to understand the superior performance of the **PTzBr** (**3**) device.

1. Introduction

The unprecedented improvement in the power conversion efficiencies (PCEs) of tin-based perovskite solar cells (TPSCs) has led to them becoming promising contenders for use in cost-effective photovoltaic devices. The theoretical PCE limit for tin-based perovskite solar cells has been estimated to be over 30%.[1,2] In recent years, a rapid improvement in the PCEs of tin-based perovskite solar cells has been observed, increasing from approximately 6% to over 14%,[3–7] with the use of hydrophilic poly(3,4-ethylenedioxylenethiophene):poly(styrene sulfonic acid) (PEDOT:PSS) as a hole-transport material (HTM). PEDOT:PSS is hygroscopic and this can lead to the quick degradation of device performance, especially in the presence of oxygen and moisture.[8] The resultant rapid oxidation from Sn^{2+} to Sn^{4+} causes the formation of Sn vacancies, due to their low formation energy,[9] leading to severe recombination losses; this is a major challenge affecting the development of TPSCs.[10] Many research articles have been published highlighting the replacement of PEDOT:PSS with different low-cost HTMs, like pyrrolopyrrole-based (PPr) polymers[11] and triphenylamine-based (TPA) polythiophenes,[12] which have excellent hole extraction capabilities, PCEs of 7.6% and 8.6%, respectively.

Among the available options, self-assembled monolayer (SAM) molecules have recently gained significant attention due to their potential to address these challenges *via* optimizing the interfacial charge transfer process through the formation of a permanent dipole moment, which can effectively modulate the work function and minimize charge recombination at the interface.[13–15] Moreover, SAMs have a higher binding affinity for hydrophobic surfaces, which reduces defect sites at the electrode, improving the perovskite crystal growth and enhancing the device performance of TPSCs.[16,17] The anchoring groups in SAMs play a crucial role in the performance and stability of PSCs. Common anchoring groups include phosphonic acid (PA), carboxylic acid (CA), and dicyanovinyl (MN) moieties, among others. Among these, PA groups are widely used; some examples of PA-anchored organic molecules for Pb-PSCs that

[a]Department of Applied Chemistry and Institute of Molecular Science, Center for Emergent Functional Matter Science, National Yang Ming Chiao Tung University, 1001 Ta-Hseuh Rd., Hsinchu 300093, Taiwan. E-mail: diau@nycu.edu.tw

[b]Department of Chemistry and Research Center of New Generation Light Driven Photovoltaic Modules, National Central University, Taoyuan 32001, Taiwan. E-mail: mcchen@ncu.edu.tw

[c]Institute of Physics, University of Rostock, Albert-Einstein-Str. 23, 18059 Rostock, Germany. E-mail: waqas.pervez@uni-rostock.de

[d]Department of Materials Science and Engineering, National Taiwan University, Taipei 10617, Taiwan

† Electronic supplementary information (ESI) available. CCDC 2383214 and 2389332. For ESI and crystallographic data in CIF or other electronic format see DOI: https://doi.org/10.1039/d4ta07975b

‡ Atika Abid and A. Velusamy contributed equally to this work.

were reported previously are shown in Fig. 1. For instance, the dimethoxydiphenylamine-substituted carbazole **V1036** was first designed by Magomedov *et al.* and used as a dopant-free hole-transporting SAM, achieving a PCE of 17.8%.[18] Ashouri *et al.* designed and synthesized carbazole-based **MeO-2PACz** and **2PACz** SAMs, with C2 alkyl chains attached to the phosphonic acid groups, which exhibited PCEs of 20.4% and 20.9%, respectively, when implemented in Pb-based inverted PSCs.[19] Li *et al.* synthesized **TPT-P6** with a phenothiazine head group and a PA anchoring group, which resulted in an increased PCE of 21.4% and enhanced stability, retaining 90% of the initial performance after three months.[20] A separate Li *et al.* group developed the simple and robust self-assembled hole-selective materials **2BrPTZPA** and **2BrPXZPA**, which feature a butyl spacer linker and Br substituents as side groups. These materials achieved high PCEs of 22.06% and 22.93%, respectively, in inverted Pb-PSCs.[21] Similarly, Ullah *et al.* synthesized a phenothiazine-based **Br-2EPT** SAM that minimizes nonradiative recombination losses, leading to an improved PCE of 22.44%.[22] Furthermore, Jiang *et al.* developed carbazole-derived helical π-expanded **CbzNaph**, which formed a densely packed and ordered monolayer, and thus resulted in an excellent PCE of 24.1 % with increased stability.[23] Wu *et al.* recently developed bisphosphonate-anchored indolocarbazole (**IDCz**)-derived SAMs, achieving a highest PCE of 25.15% for **IDCz-3**; it acts as a hole-collecting layer in inverted Pb-PSCs.[24] A new amphiphilic SAM was developed by Zhang *et al.*, with a cyanovinyl **PA** anchoring group that creates a superwetting underlayer for perovskite deposition. This results in high-quality perovskite films with fewer interfacial defects, leading to **MPA-CPA**-based PSCs with a PCE of 25.2% in Pb-PSCs.[25]

In addition, the chemical structures of some SAMs used in TPSCs are given in Fig. 1, with various anchoring groups, such as –PA, –CN, and –COOH. One of the promising SAMs, **MeO-2PACz** attained a PCE of 6.5% in TPSCs.[26] We recently used commercially available small organic molecules, specifically 4-aminobenzoic acid, as an effective SAM on ITO surfaces, enhancing charge extraction and reducing carrier recombination to achieve a higher PCE of 7.6%. Remarkably, the device exhibited impressive long-term stability, retaining approximately 80% of its initial efficiency after being in a glovebox for over 3500 h.[27] Recently, a **TP-MN** SAM based on a thieno[3,4-*b*]pyrazine core was developed by our group and a highest PCE of 7.7% was reported in combination with NiO_x in TPSCs.[28] Furthermore, X-shaped quinoxaline-based organic dyes (**TQxD**) with an extended π-conjugated thiophene component were also synthesized to align with the energy levels of tin perovskites. These dyes were employed as hole-selective SAMs in TPSCs, achieving a PCE of 8.3%.[29]

Phenothiazine is a well-known, electron-rich, and cost-effective heterocyclic compound containing nitrogen and sulfur heteroatoms. It has proven to be an outstanding building

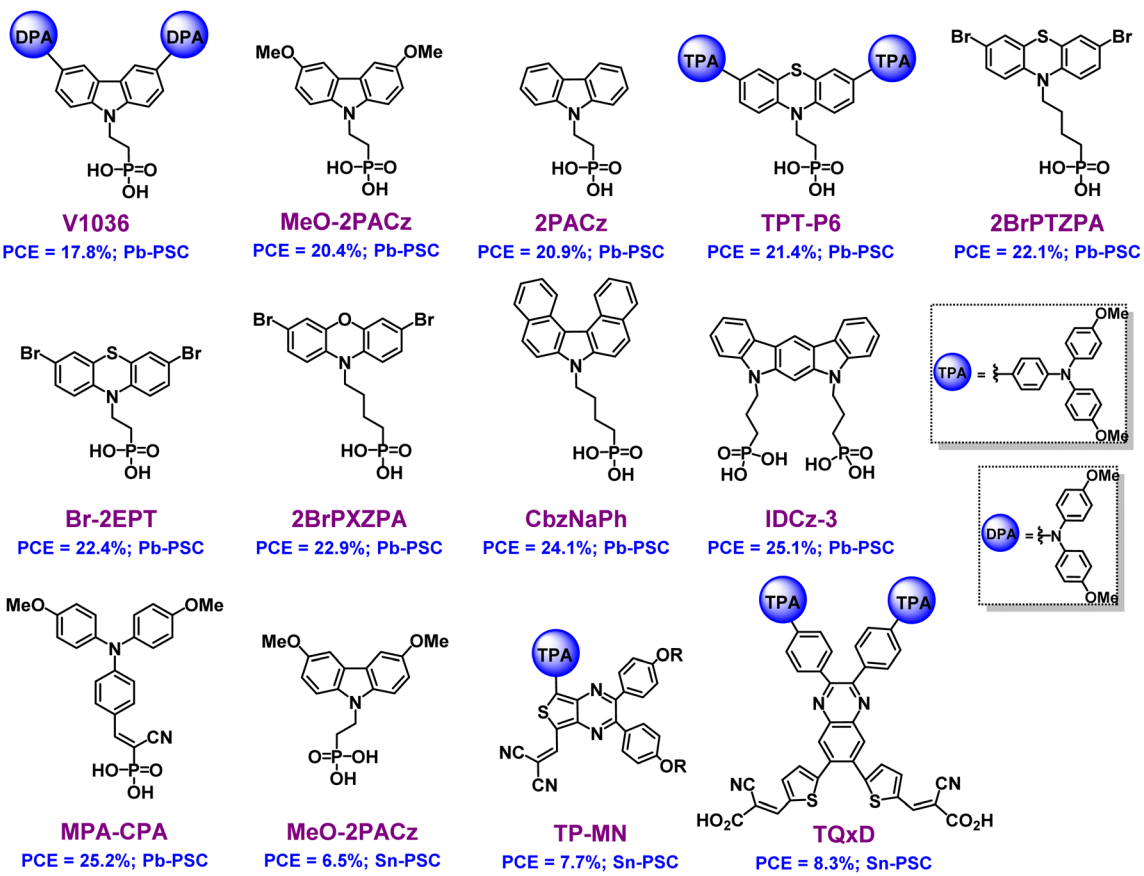

Fig. 1 The chemical structures of previously reported organic SAM molecules for use in Pb-PSCs and TPSCs.

block for high-performing HTMs in Pb-PSCs. By utilizing the advantages of the phenothiazine backbone and **PA** anchoring group, we synthesized and employed three organic materials as SAMs: **PTz**^{2} (**1**), **PTz** (**2**) and **PTzBr** (**3**). In **PTzBr** (**3**) and **PTz** (**2**), the PA groups are conjugated with the phenothiazine core *via* a butyl-substituent linker chain, while in **PTz**^{2} (**1**), they are conjugated *via* an ethyl-substituent linker chain. Highly electronegative bromine atoms are attached to the phenyl rings at *ortho* positions in the **PTzBr** (**3**) SAM to serve as terminal groups for bonding with the active tin perovskite layer, facilitating charge transport. Furthermore, single crystal analysis of **PTz** (**2**) and **PTzBr** (**3**) SAMs corroborates that the presence of intramolecular interactions and the strong binding nature of the **PA** groups could facilitate the formation of a uniform and dense SAM on the ITO substrate, promoting efficient charge transport. These SAMs were utilized on ITO substrates in combination with mixed cations in the active layer, with the best co-cationic tin perovskite having the structure of $FA_{0.75}GA_{0.25}SnI_3$. The presence of larger ammonium cations prevents moisture diffusion into the perovskite layer and provides improved grain passivation. Consequently, the **PTzBr** (**3**) SAM-based FA/GA TPSC device showed the best performance, with a PCE of 7.8% and negligible hysteresis effects. The **PTzBr** (**3**) devices also displayed remarkable long-term storage stability, maintaining about 80% of their initial efficiency for over 4000 h without encapsulation, along with light-soaking stability under one sun illumination for 9 h at the maximum power point. The thermal, morphological, optical, electrochemical, and charge recombination properties of the phenothiazine-based SAMs (**1–3**) were also evaluated.

2. Results and discussion

2.1. Synthesis

The synthetic pathway to the phenothiazine-based SAM molecules is given in Scheme 1. Firstly, the alkylated phenothiazines **4** and **6** were prepared using dibromoethane and dibromobutane, respectively, along with sodium hydride in dimethylformamide solvent. Further, the dibromination of compound **6** *via* the addition of bromine in acetic acid yields compound **8**. The bromo-/alkyl-substituted compounds (**4**, **6**, and **8**) undergo the Michaelis–Arbuzov reaction with triethyl phosphite to afford the intermediate ester compounds (**5**, **7**, and **9**). Furthermore, the phosphonates are converted to phosphonic acid derivatives using bromotrimethylsilane in dioxane, yielding the target phenothiazine-based compounds (**1–3**) in good yields (90%). These compounds are suitably soluble in common organic solvents. Furthermore, structural characterizations of all the target compounds were performed using ^{1}H, ^{13}C, and ^{31}P NMR spectroscopy and mass spectrometry, and the results are shown in Fig. S1–S21 in the ESI.†

2.2. Physical characterization

Table 1 summarizes the physical characteristics of the phenothiazine-based SAM molecules **1–3**. Thermal analyses of the newly synthesized SAM molecules were performed using thermogravimetric analysis (TGA) (Fig. S22†). TGA scans revealed that all three compounds possess good thermal stability, with ~5% weight loss temperatures of 209 °C, 227 °C, and 211 °C for **1–3**, respectively. In addition, compound **2** possesses the highest melting temperature and, thus, the highest thermal stability of

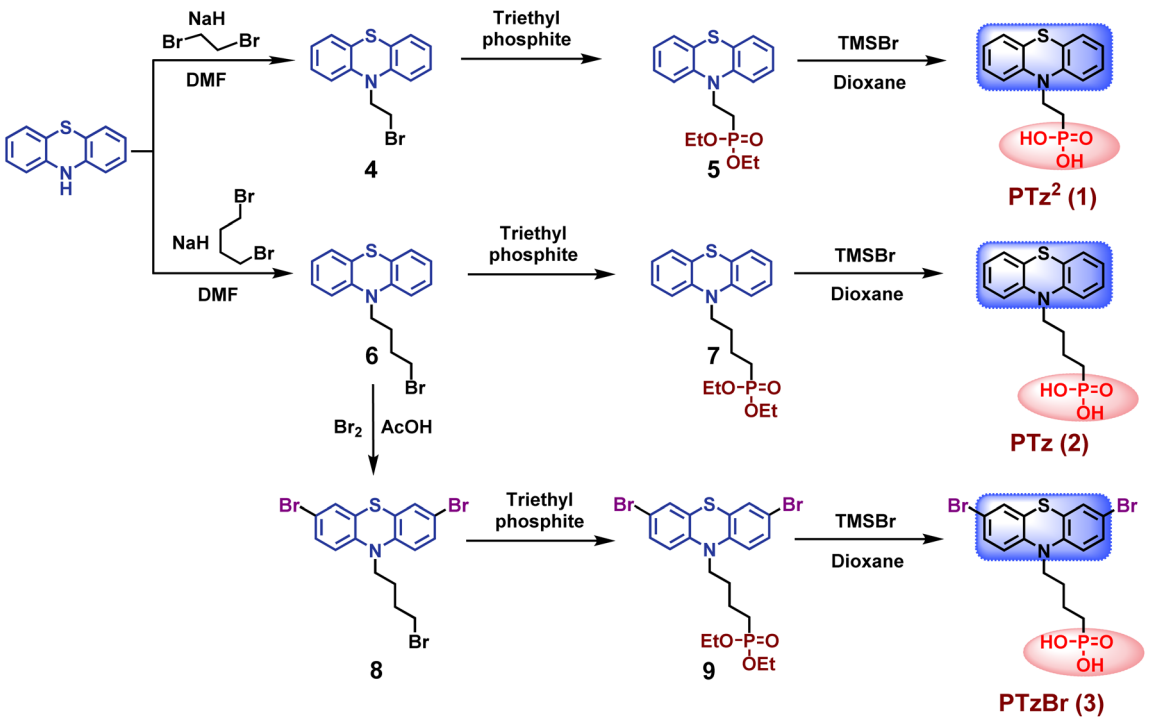

Scheme 1 The synthetic route to the phenothiazine-based SAM molecules **1–3**.

Table 1 Physical characterization data for the phenothiazine-based SAMs

Compound	T_d[a] [°C]	T_m[b] [°C]	λ_{max} (sol)[c] [nm]	ΔE_g[d] [eV]	E_{ox}[e] [V]	HOMO[f] [eV]	LUMO[f] [eV]	ΔE_g[g] [eV]
PTz² (**1**)	209	157	311	3.30	0.87	−5.31	−2.01	4.37
PTz (**2**)	227	188	311	3.37	0.83	−5.27	−1.90	4.34
PTzBr (**3**)	211	180	319	3.18	1.02	−5.46	−2.28	4.20

[a] Based on TGA. [b] From melting point apparatus data. [c] Determined in *o*-DCB. [d] Calculated based on $1240/\lambda_{abs}$ (onset). [e] From DPV in *o*-DCB. [f] HOMO/LUMO = $-(4.44 + E_{ox}/E_{red})$ *vs.* NHE. [g] $\Delta E_g = E_{LUMO} - E_{HOMO}$ from DFT calculations.

the series. This can be attributed to the efficient packing and stronger intermolecular interactions, resulting in higher melting and decomposition temperatures compared to other compounds.[30] The optical absorption properties of all three compounds were measured in *o*-dichlorobenzene (*o*-DCB) solutions. Fig. 2a shows the UV–vis absorption spectra, which exhibit identical peak maxima (λ_{max}) at 311 nm for compounds **1** and **2**, while that of compound **3** is slightly redshifted to 319 nm due to the presence of electronegative bromine atoms. The optical bandgaps, extracted from the absorption onset values of

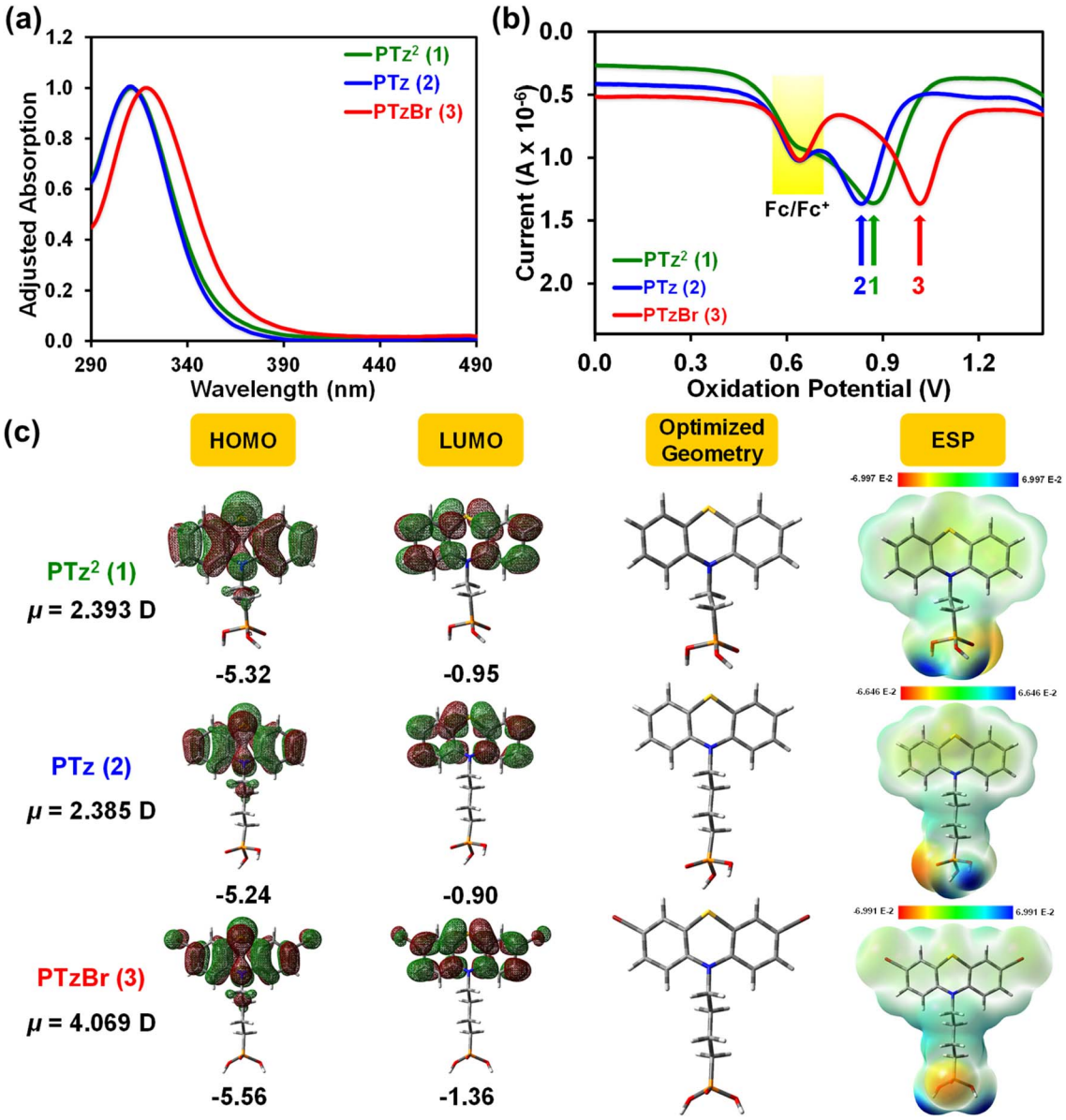

Fig. 2 (a) UV-vis absorption spectra; (b) DPV curves; and (c) DFT-derived energy levels, dipole moments, and electrostatic surface potential (ESP) mapping of the PTz-based compounds.

the spectra, are 3.30 eV, 3.37 eV, and 3.18 eV, respectively, for compounds **1–3**. Consequently, changing the alkyl chain substituent results in similar optical properties and does not significantly affect the π-conjugated backbone for compounds **1** and **2**, while compound **3** shows a smaller energy gap value due to the presence of electronegative bromine atoms. Differential pulse voltammetry (DPV) was performed in *o*-DCB at 25 °C to examine the electrochemical characteristics of the SAM molecules **1–3** (Fig. 2b and S23†), using tetrabutylammonium hexafluorophosphate as the electrolyte.[31,32] Ferrocene served as an internal standard to calibrate the oxidation potentials of the SAMs **1–3**, with a reference potential of +0.64 V. The equation $E_{HOMO} = -(4.44 + E_{ox})$ was used to calculate the HOMO energy levels of the SAM molecules **1–3**. The first oxidation peaks of compounds **1–3** are located at +0.87, +0.83, and +1.02 V, resulting in E_{HOMO} values of −5.31 eV, −5.27 eV, and −5.46 eV, respectively. Due to the shorter ethyl alkyl chain in compound **1**, the electron-withdrawing PA group was positioned closer to the phenothiazine core and, hence, was harder to oxidize compared to compound **2** with a longer alkyl chain substituent. As expected, compound **3** shows the lowest HOMO among the series due to the presence of electronegative bromine atoms.

2.3. Theoretical calculations

To investigate the electronic structures of the phenothiazine-based SAMs, DFT calculations were employed at the B3LYP/6-31G* level of theory using Gaussian 09W software (Fig. 2c). The HOMOs and LUMOs were primarily located on the conjugated part, with the HOMO partially extending to the alkyl chain.[21] Benefiting from the electronegative Br atoms, compound **3** exhibits an increased dipole moment (μ) and stronger electron-withdrawing properties compared to compounds **1** and **2**. This leads to a lower HOMO energy level for compound **3**. The calculated μ values are 2.393 D, 2.385 D, and 4.069 D for the SAMs **PTz2** (**1**), **PTz** (**2**), and **PTzBr** (**3**), respectively. Due to its larger dipole moment and lower HOMO energy level, **PTzBr** (**3**) demonstrates efficient hole extraction in an ITO/**PTzBr** system. The DFT-derived E_{HOMO} and E_{LUMO} values for compounds **1**−**3** are −5.32/−0.95 eV, −5.24/−0.90 eV, and −5.56/−1.36 eV, respectively. The corresponding energy gap values are provided in Table 1. Notably, the energy gaps determined through computational, optical, and electrochemical methods are nearly comparable, indicating the consistency of these values. Additionally, electrostatic potential (ESP) surface analysis of the phenothiazine-based SAMs was performed to analyze the molecular charge distributions and examine the interactions between ITO and the anchoring group sites (Fig. 2c). DFT calculations from the ESP mapping images of the three SAMs indicate that a high density of negative charge is predominantly located on the oxygen atom of the **PA** anchoring groups. This facilitates strong interactions between the SAMs and the ITO substrate *via* the anchoring groups, potentially enhancing charge transport at the ITO/SAM/perovskite interfaces in TPSCs.

2.4. Single crystal structures

To obtain further insight into the structures of the SAM molecules, single crystals of **PTz** (**2**) and **PTzBr** (**3**) were grown *via* the slow solvent evaporation of methanol. The diffraction-derived single crystal structures of the molecules are presented in Fig. 3 and S24;† the corresponding crystal data are provided in Tables S1 and S2.† These results indicate that the **PTz** (**2**) molecule crystallizes in an orthorhombic system with the *Iba*2 space group, whereas the **PTzBr** (**3**) molecule crystallizes in a monoclinic system with the *C*2/*c* space group. Fig. 3a and b illustrates intramolecular distances of 2.83–2.84 Å for S···H, and 2.67–2.62 Å for N···H, with three oxygen atoms (attached to P) serving as anchoring points. These interactions could facilitate the formation of highly ordered SAMs on the substrate with a dense and tilted texture. The dihedral angles between the planes of the two benzene rings are ∼133°, indicating that the **PTz** core bends by about ∼46° (Fig. 3c and d). As shown in Fig. 3e and f, the short C–P distances of 1.77 to 1.78 Å and short N···H (alkyl) distances of 2.01 to 2.02 Å for both SAMs facilitate efficient charge transport through the phosphonic acid anchoring groups. Furthermore, the proposed packing patterns for the SAM molecules on the ITO substrate are demonstrated in Fig. 3g and h, promoting charge transfer efficiency and allowing high-performance TPSCs. With respect to this crystallographic information, the single-crystal structures of **PTz** (**2**) and **PTzBr** (**3**) exhibit similarities. However, the introduction of bromine enhances intermolecular interactions, promotes planarity, and facilitates favorable packing arrangements. These factors contribute to more efficient charge transport and ultimately suggest that the dibromo-SAM molecule, **PTzBr** (**3**), could achieve greater device performance in TPSCs.

2.5. Thin-film characterizations

We further explore the surface properties of the phenothiazine-based SAMs **PTz^2** (**1**), **PTz** (**2**), and **PTzBr** (**3**), with a particular emphasis on their wettability. We first produced the SAMs on ITO substrates by employing a dipping method. Our previous study indicates that the performance of the dipping method is better than the conventional spin-coating method, promoting strong covalent bonding between the respective SAM and ITO substrate. This induces the formation of an atomically thin, self-organized functional layer with improved coverage and robust adhesion.[27] Thereafter, the contact angle was measured after dropping the SnI_2/DMSO precursor on the SAM (**1–3**)-coated ITO substrates. The contact angles are shown in Fig. 4a–c for ITO/**PTzBr** (**3**) (∼6.10°), ITO/**PTz** (**2**) (∼7.36°), and ITO/**PTz^2** (**1**) (∼9.46°), respectively. In the case of ITO/**PTzBr** (**3**), higher wettability and a smaller contact angle were observed due to the electronegative and polar nature of the bromine atoms, which facilitates strong halogen bonding interactions with the precursor solution for this SAM. However, slightly higher contact angles were observed for the other two SAMs, which may be attributed to an absence of electronegative components, which could cause higher surface tension and lower wettability. To investigate the presence of atomic species from the SAMs on ITO and to compare the results with the bare ITO substrate, we performed X-ray photoelectron spectroscopy (XPS) measurements. Fig. S25a–d† presents the XPS spectra of the SAMs **1–3**; four distinct components labeled Br 3d, N 1s, P 2p, and S 2p

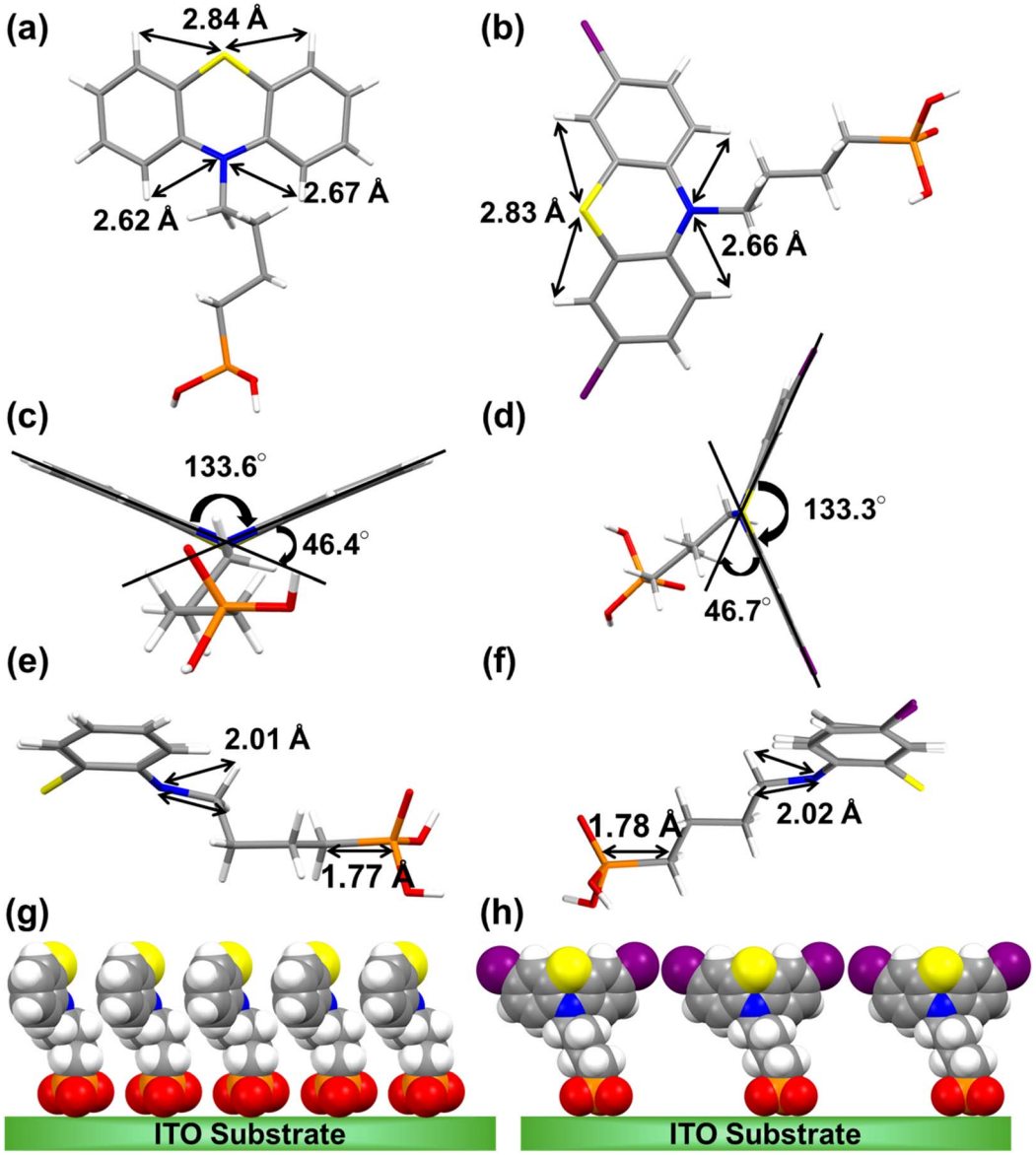

Fig. 3 The single crystal structures of the SAMs **PTz** (**2**) and **PTzBr** (**3**). (a and b) Top–down views of molecules **2** and **3** in stick-model form showing intramolecular interactions; (c and d) front views of molecules **2** and **3** in stick-model form showing dihedral angles; (e and f) side views of molecules **2** and **3** in stick-model form; and (g and h) the proposed packing patterns of SAMs on the ITO substrate represented using a space-filling model. (a), (c), (e), and (g) Correspond to **PTz** (**2**), while (b), (d), (f), and (h) correspond to **PTzBr** (**3**).

were deconvoluted from the original data. The **BrPTz** (**3**) SAM exhibited a clearly discernible shoulder peak at a lower binding energy (~71 eV), which showed that the phenothiazine core is an electron-rich heterocyclic compound due to the presence of nitrogen and sulfur atoms. These atoms can donate electron density through resonance or inductive effects to the bromo groups located at the *ortho* positions of the aromatic ring (Fig. S25a†). Other species such as N, P, and S were also detected with comparatively higher binding energies for all the SAMs (Fig. S25b–d†). These results indicate that the successful functionalization of SAMs, through the anchoring phosphonic acid group, onto ITO substrates results in compact and uniform monolayers *via* a self-limiting process.[22] Once SAM molecules are adsorbed onto the ITO surface, their anchoring groups, such as phosphonic acid, form strong covalent bonds with the substrate. This bonding is attributed to the high adsorption energy of the phosphonic acid group on the ITO surface.[33] These covalent bonds are generally robust enough to withstand short-term UV-O_3 treatment. However, due to spatial constraints, some SAM molecules may struggle to achieve close proximity to the ITO surface, preventing the formation of strong bonds. These molecules can contribute to the formation of organic contaminants or an oxide layer, which, in turn, can create hydrophobic patches. Such effects often lead to the molecular aggregation or incomplete spreading of the SAM layer.

Applying UV-O_3 treatment after the adsorption of SAM molecules proves to be an effective strategy to address these challenges. This process increases the surface energy of SAM-

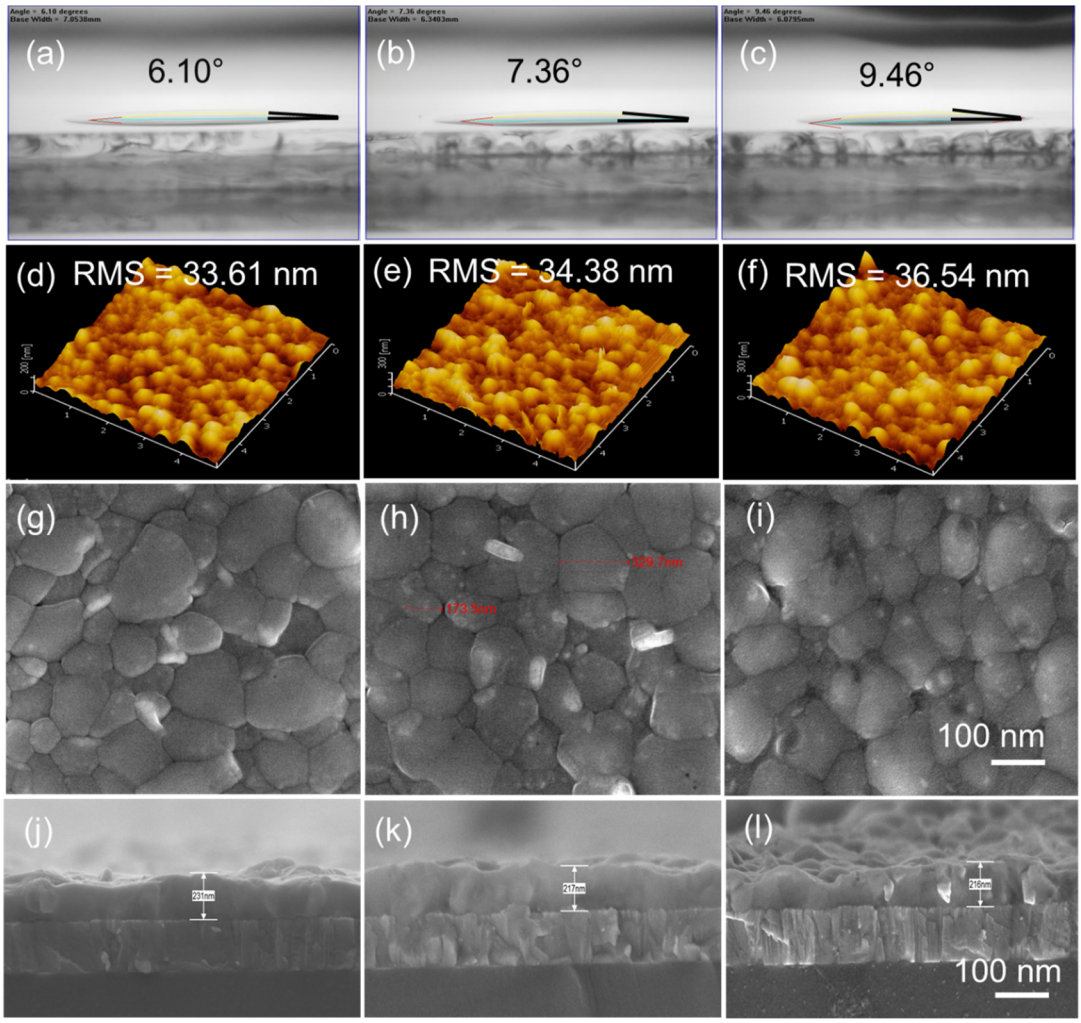

Fig. 4 Contact angles of the perovskite precursor SnI_2/DMSO solution measured on the phenothiazine-based SAMs **1–3** coated on ITO substrates (a–c); and AFM roughness images (d–f), SEM top-view images (g–i), and SEM cross-sectional images (j–l) of $FA_{0.75}GA_{0.25}SnI_3$ -based perovskite films prepared on the phenothiazine-based SAMs **PTz**^{2} (**1**), **PTz** (**2**), and **PTzBr** (**3**) coated on ITO substrates. (a), (d), (g), and (j) Correspond to **1**; (b), (e), (h), and (k) correspond to **2**; and (c), (f), (i) and (l) correspond to **3**.

coated ITO, enhancing its hydrophilicity. Consequently, the wetting behavior of SAM molecules allows them to spread more uniformly and attach more effectively. This is evidenced by a reduction in the contact angle after UV-O_3 treatment, as shown in Fig. 4a–c, indicating better surface coverage and band alignment. Moreover, UV-O_3 treatment facilitates the realignment of loosely bound or aggregated SAM molecules, leading to the formation of a more uniform and well-ordered monolayer. These improvements in surface properties demonstrate that post-adsorption UV-O_3 treatment not only preserves the integrity of the adsorbed SAM layer but also enhances its uniformity and functional performance.

In our previous study,[34] we showed that the mixed cations in tin perovskite significantly impacted the device's performance. Hence, we systematically examined device performance upon incorporating the organic cations GA and MA at the A-site position of ABX_3 to form mixed cations with FA, in the form of $FA_xA_{1-x}SnI_3$ (FA/A), during the deposition of tin perovskite film on SAM-coated ITO substrates according to a two-step fabrication method reported previously.[26,35,36]

Fig. S26† shows AFM images depicting the almost-similar surface morphologies and roughness when the SAMs **1–3** are coated on ITO substrates. The surface roughness of the SAM-coated ITO substrates with the $FA_{0.75}GA_{0.25}SnI_3$ perovskite precursor showed distinct changes in terms of average film roughness; the values are **PTzBr** (**3**): 33.61 nm, **PTz** (**2**): 34.38 nm, and **PTz**^{2} (**1**): 36.54 nm, as shown in Fig. 4d–f. These surface roughness values increase in $FA_{0.75}MA_{0.25}SnI_3$-based perovskite films, as shown in Fig. S27a–c.† Conversely, Fig. S27j–l† shows $FASnI_3$-based perovskite films on SAM-coated ITO substrates, indicating relatively lower roughness as compared to mixed-cationic perovskites. In addition, top-view SEM images of $FA_{0.75}GA_{0.25}SnI_3$-based perovskite films on the phenothiazine-based SAMs **1–3** coated on ITO substrates (Fig. 4g–i) show improved uniformity, with tightly packed grains and reduced surface defects. Importantly, the grain size of the

GA-based perovskite deposited on the SAMs **1–3** increased as compared to the active layers grown from $FA_{0.75}MA_{0.25}SnI_3$ and $FASnI_3$ in the presence of an $EDAI_2$ and SnF_2 co-additive.

The larger grains are due to synergistic interactions and the non-linear structure of GA, which has three amidine functional groups with unsaturated nitrogen atoms that modulate the crystal growth to slow it,[37] facilitating the improved quality of the perovskite films;[38] these features result in the smoother surface of the GA/FA perovskite compared with the others. In contrast, Fig. S27d–f† exhibits perovskite films of $FA_{0.75}MA_{0.25}SnI_3$ with no obvious grain boundaries, which may lead to phase segregation and cluster formation. The poor surface morphology and inhomogeneity of the grains are due to the distinct chemical structure and interactions of the MA cation.[39] Conversely, as seen in Fig. S27m–o,† as the FA content increased, the grain boundaries became progressively more pronounced and well-aligned with the AFM images, as shown in Fig. S27j–l.† When investigating the impact of the SAMs **1–3** on the film thickness, cross-sectional SEM images revealed visible changes in the $FA_{0.75}GA_{0.25}SnI_3$-based perovskite film, as shown in Fig. 4j–l. These confirm that tin perovskite deposited on **PTzBr** (**3**) has a higher film thickness of 231 nm than the other two, **PTz** (**2**) and **PTz^2** (**1**), which show thicknesses of 217 nm and 216 nm, respectively. In comparison, Fig. S27g–i† shows the uneven thicknesses of the FA/MA-based perovskite films, which is in agreement with the SEM top-view images (Fig. S27d–f†). Meanwhile, FA-based perovskite films show a lower thickness compared to the mixed-cationic perovskites, as illustrated in Fig. S27p–r.† Further, a comparison of grain sizes extracted from SEM images of various perovskite (PSK) films fabricated using three different SAMs is represented in a bar chart (Fig. S28†).

The XRD patterns of the SAM/PSK samples, presented in Fig. S29,† display the characteristic diffraction peaks of $FA_{0.75}GA_{0.25}SnI_3$-based perovskites, with exposed facets indicated alongside the diffraction peaks of the ITO glass substrate (marked as #).[40] The diffraction peaks corresponding to the (100) planes of the **PTzBr** (**3**)-, **PTz** (**2**)-, and **PTz^2** (**1**)-based perovskite samples exhibit comparable intensities to the ITO diffraction peak at ~36°. This observation suggests not only the excellent surface coverage and appropriate thickness of the perovskite layer but also its high crystallinity. Among the samples, **PTzBr** (**3**)/PSK exhibits the sharpest (100) peak, indicating superior crystalline quality, whereas **PTz** (**2**)/PSK and **PTz^2** (**1**)/PSK show broader peaks. This trend highlights the role of Br substitution at the *ortho* position in enhancing the grain size and surface morphology of PSK film, as supported by Fig. 4g.

The optical bandgaps (E_g) extracted from UV-vis spectra and Tauc plots of $FA_{0.75}GA_{0.25}SnI_3$-based perovskite films have

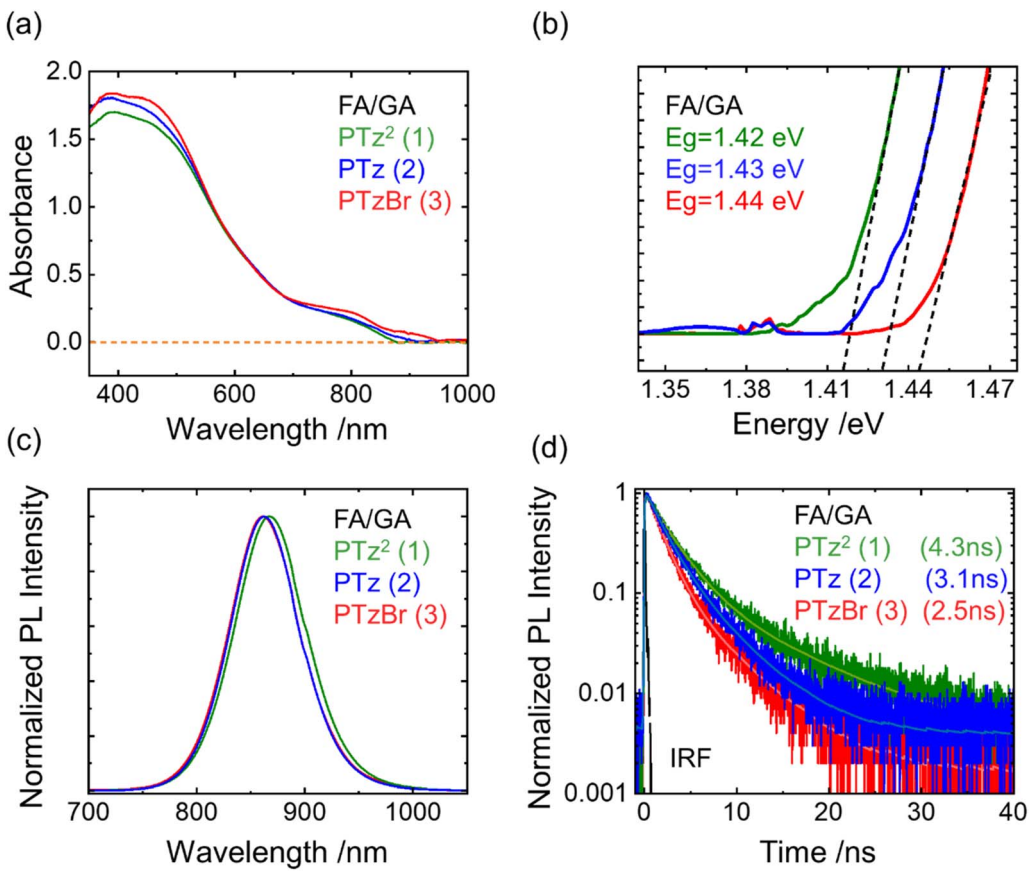

Fig. 5 (a) Ultraviolet-visible absorption spectra; (b) tauc plots diagram; (c) steady-state PL spectra; and (d) time-resolved PL decay profiles of $FA_{0.75}GA_{0.25}SnI_3$-based perovskite films formed on the phenothiazine-based SAMs **PTz^2** (**1**), **PTz** (**2**), and **PTzBr** (**3**) coated on ITO substrates.

similar band-edge positions (Fig. 5a and b), in the range of 1.42–1.44 eV. Narrow bandgaps were observed in the range of 1.37–1.39 eV for MA-based mixed cationic systems (Fig. S30a†). For $FASnI_3$ deposited on the SAMs **1–3**, the bandgaps are in the range of 1.41–1.42 eV (Fig. S30b†). To explore the quality of the active layer on the phenothiazine-based SAMs **1–3** coated on ITO substrates, we conducted steady-state photoluminescence (PL) and time-correlated single photon counting (TCSPC) measurements for the FA/GA perovskite films. The photoluminescence (PL) measurements were performed on the top surfaces of the perovskite films, with a 450 nm excitation source. The penetration depth of this wavelength into perovskite films typically falls in the range of 200–300 nm, based on reported absorption coefficients (10^4–10^5 cm^{-1}).[41] Scanning electron microscopy (SEM) images reveal the thicknesses of the films as follows: **PTzBr**: 231 nm, **PTz**: 217 nm, and **PTz^2**: 216 nm; this indicates that the excitation source interacts with the majority of the bulk perovskite layer with limited contribution from the interface. Fig. 5c shows the PL spectra, with a slight blueshift from **PTz^2** (**1**) to **PTzBr** (**3**). This blue spectral shift in PL is consistent with the trend observed in the UV-vis spectra shown in Fig. 5a. To better understand the effect of charge extraction, we analyzed the time-resolved PL spectra of encapsulated $FA_{0.75}GA_{0.25}SnI_3$ perovskite films on ITO surfaces modified with the SAMs **1–3**. This analysis allows for a comparison of charge extraction rates between the three SAMs. Fig. 5d shows that all the observed PL decay profiles do not show single exponential decay features; nevertheless, they can be fitted well using a biexponential decay function. The averaged PL lifetimes were obtained using the intensity-average method, which shows hole extraction capabilities with the following trend in the GA/FA based films: **PTzBr** (**3**) (2.5 ns) ˃ **PTz** (**2**) (3.1 ns) ˃ **PTz^2** (**1**) (4.3 ns) (Table S3†). Although the larger grains in the FA/GA system can help to reduce the density of grain boundaries and enhance the PL lifetimes,[42] the reduced PL lifetime in the tin perovskite deposited on **PTzBr** (**3**) indicates rapid hole extraction from the FA/GA perovskite to the SAM **3** which helps support efficient charge separation in TPSCs.

2.6. Device performance and characterizations

To determine the potential energy levels, ultraviolet photoelectron spectra (UPS) were measured for the SAMs **1–3** coated on ITO substrates; the corresponding results are shown in Fig. S31.† The previously reported work function of bare ITO glass is 4.7 eV.[43] This was markedly altered to 5.08 eV for ITO/**PTzBr** (**3**), 5.06 eV for ITO/**PTz** (**2**), and 5.00 eV for ITO/**PTz^2** (**1**). Therefore, we expect that the surface properties of the ITO/SAM substrates could lead to feasible modulation of the energetics of the FA/GA perovskite film. After depositing tin perovskite on the SAM substrates, UPS measurements were used to determine the energy levels of the valence band maxima (VBM) of the SAM/perovskite samples; the corresponding UPS data are shown in Fig. S32.† The estimated VBM levels for **PTzBr** (**3**)/PSK, **PTz** (**2**)/PSK, and **PTz^2** (**1**)/PSK were found to be −5.12 eV, −5.10 eV, and −5.26 eV, respectively. The conduction band minimum (CBM) values were calculated accordingly using the E_g and VBM values. Interestingly, a favourable alignment of energy levels was observed; holes could transfer from the VBM of the perovskite to the HOMO of the SAM on the ITO substrate, whereas electrons could readily transfer from the CBM of the perovskite to the LUMO of C_{60}, as depicted in Fig. 6a. Various studies have

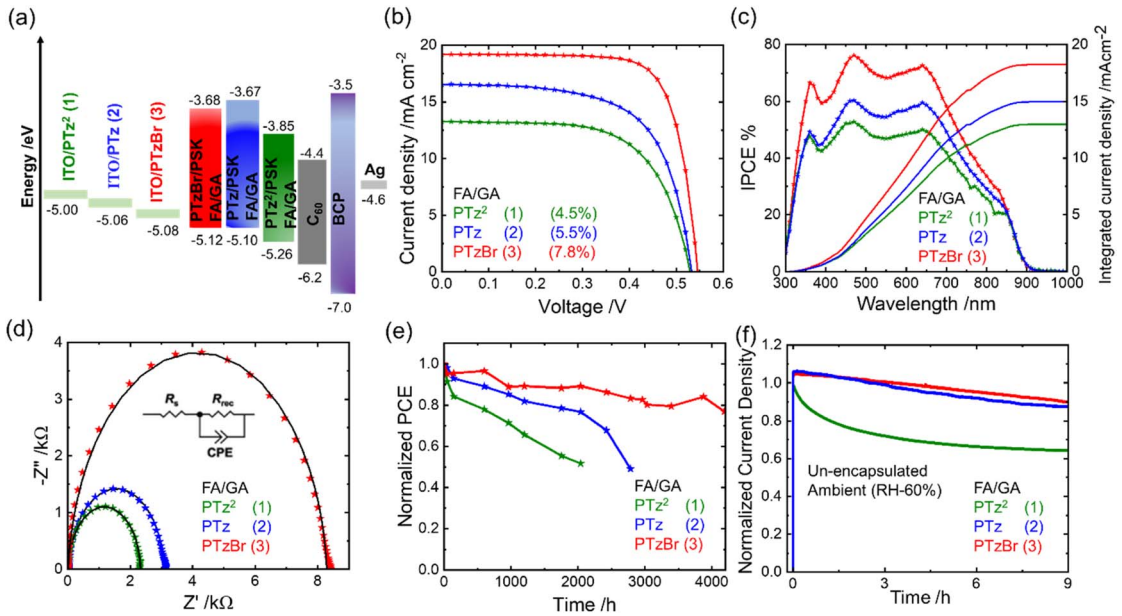

Fig. 6 (a) Energy-level diagrams based on UPS spectra, (b) *J*–*V* curves for the best devices, (c) IPCE spectra and integrated current–density curves, (d) EIS Nyquist plots, (e) the long-term stability for devices stored in a glovebox, and (f) MPP tracking during light soaking for 9 h without encapsulation under ambient conditions. The devices are made of an $FA_{0.75}GA_{0.25}SnI_3$-based perovskite precursor deposited on the SAMs **PTz^2** (**1**), **PTz** (**2**), and **PTzBr** (**3**), as indicated.

reported that the VBM values of $FASnI_3$ range from −5.2 to −6.0 eV,[44–47] which are slightly lower than our findings of −4.90 to −5.00 eV shown in Fig. S33a.† The role of MA in the presence of FA seems to be different compared to that of GA in the mixed cationic systems. $FA_{0.75}MA_{0.25}SnI_3$ showed a nonlinear dependence of the VBM on the mix proportions.[48] UPS measurements give VBM values of −5.07 eV for **PTzBr** (**1**)/PSK, −5.06 eV for **PTz** (**2**)/PSK, and −5.06 eV for **PTz^2** (**1**)/PSK, as illustrated in Fig. S34a.†

Research indicates that methylammonium (MA), known for its acidic and hygroscopic nature, undergoes protonation upon direct contact with moisture.[49–51] This interaction disrupts the bonding between the organic component at the 'A' site and the Sn atom at the 'B' site of the perovskite structure. Such bond disruption can lead to the formation of clusters within the crystal grains due to the coexistence of MA and FA, contributing to the high observed surface roughness, as previously demonstrated in Fig. S27a–c.†

Previous studies have shown that GA cations are not only integrated into the crystal structure, they are also located on the surface.[52] In this study, we observed that GA has a negligible impact on E_g and it improved the surface passivation. To assess the performance of TPSCs, inverted p–i–n structure ITO/SAM/$FA_xA_{1-x}SnI_3$/C60/BCP/Ag devices were fabricated using a two-step fabrication method reported previously.[53] Fig. 6b presents the current density–voltage (J–V) curves for the best $FA_{0.75}GA_{0.25}SnI_3$ tin perovskite solar cell devices measured under standard AM 1.5 G illumination. The best-performing device including **PTzBr** (**3**) exhibited a remarkably high PCE of 7.8% in the reverse scan direction, with a V_{OC} value of 0.548 V, a J_{SC} value of 19.19 mA cm^{-2}, and a FF of 0.747; the other two devices, incorporating **PTz** (**2**) and **PTz^2** (**1**), had PCEs of 5.5% and 4.5%, respectively. The corresponding photovoltaic parameters are listed in Table 2. The $FA_{0.75}GA_{0.25}SnI_3$-based devices showed hysteresis-free behavior between reverse (V_{OC} to 0 V) and forward (0 V to V_{OC}) scans, as shown in Fig. S35.† Consistent behaviour is displayed based on the PCEs obtained from J–V sweeps. In particular, the higher V_{OC}, J_{SC}, and FF values of the devices fabricated on **PTzBr** (**3**) suggest that the introduction of electronegative Br atoms into the phenothiazine backbone could potentially increase the π-conjugation, which helps to passivate some iodine vacancies at the buried SAM/PSK interface. Through spectral deconvolution, the relative proportions of Sn^{2+} and Sn^{4+} oxidation states were determined, and the corresponding results are shown in Table S4.† Accordingly, as seen in Fig. S36,† **PTzBr** (**3**)/PSK possessed the highest Sn^{2+}/Sn^{4+} ratio (82.7/17.3), followed by **PTz** (**2**)/PSK (81.8/18.2) and **PTz^2** (**1**)/PSK (80.2/19.8), while the lowest Sn^{2+}/Sn^{4+} ratio (68.7/31.3) was seen in the ITO/PSK sample. These findings indicate that bromine in **PTzBr** interacts with uncoordinated Sn atoms, facilitating the formation of a passivating layer. This passivation mechanism effectively mitigates surface defects and recombination pathways, thereby contributing to improved material stability and device performance.

Table 2 The photovoltaic parameters of the best-performing $FA_{0.75}GA_{0.25}SnI_3$ devices based on the results from J–V curves in Fig. 6b

Device	V_{OC}/V	J_{SC}/mA cm^{-2}	Integrated J_{SC}	FF/%	PCE/%
PTz^2 (**1**)	0.534	13.27	13.18	0.637	4.5
PTz (**2**)	0.539	16.53	15.19	0.621	5.5
PTzBr (**3**)	0.548	19.19	18.49	0.747	7.8

To confirm the effects of **PTzBr** on carrier mobility, space-charge-limited current (SCLC) measurements were conducted. The results shown in Fig. S37† suggest that **PTzBr** indeed improves the extraction of photogenerated carriers compared to the other two SAMs. **PTzBr** may passivate surface defects within the perovskite layer or at the interfaces, thereby reducing trap-assisted recombination. This passivation process increases the number of free carriers available for current generation. Furthermore, as seen in Fig. 6c, $FA_{0.75}GA_{0.25}SnI_3$-based devices show integrated J_{sc} values of 18.5 mA cm^{-2}, 15.2 mA cm^{-2}, and 13.2 mA cm^{-2}, as obtained from the incident-photon-to-current efficiency (IPCE) spectra, validating the current values obtained from the J–V scans (Fig. 6b). The photovoltaic characteristics of $FASnI_3$ and $FA_{0.75}MA_{0.25}SnI_3$ devices are shown in Fig. S33 and S34,† respectively; the corresponding photovoltaic parameters are summarized in Tables S5 and S6.† The overall absorption spectra of SAM/PSK films in the range of 350 to 900 nm align well with the perovskite film thicknesses in terms of the photocurrents, with a decreasing trend of **PTzBr** (**3**) > **PTz** (**2**) > **PTz^2** (**1**); this is reflected in the IPCE spectra, which show the same response.

We also fabricated 25 devices using each SAM (**1**–**3**) under identical experimental conditions in different batches with an active area of 0.0225 cm^2 to investigate the reproducibility of the FA/GA-based devices; the corresponding photovoltaic parameters are listed in Tables S7–S9.† Fig. S38† shows a statistical analysis of the data obtained from the boxplots, which reveals the high reproducibility of our devices. To evaluate the extent of carrier recombination[54] and the ionic processes involving the mixed cations in the devices, we also carried out electrochemical impedance spectroscopy (EIS) measurements under darkness. The EIS measurements were conducted by applying a bias voltage at V_{OC} with an amplitude of 10 mV in the frequency range of 1–1M Hz. Fig. 6d and S33c and S34c† show the Nyquist plots for FA/GA-, FA-, and FA/MA-based devices, respectively. The EIS data were fitted by applying an appropriate equivalent-circuit model with the parameters of series resistance (R_s), recombination resistance (R_{rec}), and a constant phase element (CPE); the corresponding R_s and R_{rec} values are outlined in Table S10.† A higher R_{rec} value at increased applied voltages can contribute to a higher V_{OC}.[55] The charge recombination resistances of these devices show a systematic trend in the order **PTzBr** > **PTz** > **PTz^2** for all three (FA/GA, FA/MA, and FA) systems; this is in good agreement with the V_{OC} values, which show the same order. The **PTzBr**-based device has the best performance in the FA/GA system with the largest R_{rec} value at a high applied voltage of 0.548 V. This could be due to the extension of the π-conjugation system of the Br group towards the chain of the sigma bond, allowing a hyperconjugation effect that works efficiently in the hole-extraction process and reduces

the non-radiative recombination through the mixing of cations to improve the device performance, as per the results shown in Fig. 6b.

Earlier studies on the stability of tin perovskite suggested that the incorporation of larger ammonium cations such as GA enhances the hydrophobicity of films and impedes moisture diffusion into the perovskite layer.[56] In addition, GA has effects on grain passivation and can effectively annihilate surface defects to improve the film morphology, as shown in Fig. 3g–i. To prove this, we studied the enduring stability of the FA/GA-based devices stored in a nitrogen-filled glovebox; the corresponding results are shown in Fig. 6e. Specifically, the **PTzBr** device has outstanding long-term stability, maintaining 80% of its original PCE for over 4000 h. Problems with the long-term stability of TPSCs are the main obstacle when promoting the performance of these devices. To address this point, we monitored the stability of $FA_{0.75}GA_{0.25}SnI_3$-based devices stimulated under one sun illumination at the maximum power point (MPP) under ambient air conditions (~60% relative humidity) without encapsulation for 9 h. As seen in Fig. 6f, **PTzBr**, and **PTz** cells retained 90% and 85% of their initial efficiencies, respectively, after continuous soaking at the MPP. The study of steady-state output data at the MPP for 600 s was conducted to provide a focused analysis of the device's short-term stabilization and its consistent performance under controlled conditions. This short-term analysis can provide additional insights into the device's immediate stabilization behavior and performance under controlled conditions. By correlating the short-term (600 s) and long-term (9 h) data, we validate the reliability and robustness of the device. The results of the 600 s test are provided in Fig. S39.† The ethyl-substituent linker chain in **PTz²** degrades quickly under illumination in comparison to the butyl substituent as a linker chain. This is consistent with the TCSPC results showing that a greater number of aliphatic carbon chains can help support efficient charge separation and reduce charge recombination at the interface.[57]

Notably, we investigated the mixing of A-site cations in SAM-based devices for the first time, suggesting further avenues for improving the efficiencies of TPSCs. Our work deepens the understanding of the role of larger-size GA in SAM-based devices and also contributes to improvements in PCE and stability, which are mainly achieved by modifying the surface energy level, reducing interfacial defects, enhancing the quality of perovskite films, and preventing device degradation. As a result, the **PTzBr** device displayed outstanding performance in the FA/GA system because of rapid charge extraction, retarded charge recombination, grain surface passivation, reduced interfacial trap defects, and excellent band-energy alignment.

3. Conclusions

We designed and synthesized three phenothiazine-based SAM molecules, **PTz²** (**1**), **PTz** (**2**), and **PTzBr** (**3**), for use in tin-based perovskite solar cells. Phenothiazine is a well-known, electron-rich, and heterocyclic compound containing nitrogen and sulfur heteroatoms. The phosphonic acid groups are conjugated with the phenothiazine moiety *via* a butyl-substituent linker chain in **PTzBr** (**3**) and **PTz** (**2**), and *via* an ethyl-substituent linker chain in **PTz²** (**1**). Highly electronegative Br atoms are conjugated with the phenyl ring at *ortho* positions in the **PTzBr** SAM to serve as terminal groups that can bond with the active perovskite layer for electron donation. The single crystal structures of **PTz** (**2**) and **PTzBr** (**3**) reveal similarities; however, the introduction of bromine substituents into the latter compound significantly alters its packing and intermolecular interactions. These structural changes enhance charge transport and optimize the energy-level alignment, leading to a higher PCE compared to the non-brominated analogs. For the first time, we explored the mixing of A-site cations in phenothiazine-based SAM devices, opening up new possibilities for improving TPSC performance. Our work deepens the understanding of the role of larger-size GA in the FA/GA system and contributes to improvements in PCE and stability. This is mainly achieved by modifying the surface energy level, reducing interfacial defects, enhancing the quality of perovskite films, and preventing device degradation compared to devices prepared with FA and FA/MA systems. As a result, we found that the phenothiazine-based SAM devices displayed better performance, with the FA/GA system showing a PCE trend of **PTzBr** (7.8%) > **PTz** (5.5%) > **PTz²** (4.5%). We also performed AFM, SEM, UPS, TCSPC, and EIS characterizations to deeply investigate the surface and optoelectronic properties of perovskite films when utilizing this series of SAMs. It is noteworthy that the device fabricated with the **PTzBr** SAM demonstrated excellent long-term stability, retaining ~80% of its original performance after 4000 h of shelf storage. This device featured rapid charge extraction, retarded charge recombination, reduced interfacial trap defects, and improved energy-band alignment. Our results also indicate that synergy between different cations offers a promising research avenue for allowing TPSCs to attain high performance and outstanding stability through SAM-based devices.

Data availability

The data supporting this article have been included as part of the ESI.†

Conflicts of interest

There are no conflicts to declare.

Acknowledgements

We thank Pei-Lin Chen (Instrumentation Center at NTHU) for single crystal X-ray diffractometer analysis. We gratefully acknowledge the support of the National Science and Technology Council (NSTC), Taiwan (grant No. NSTC 111-2622-8-008-006, NSTC 112-2639-M-A49-001-ASP and NSTC 113-2639-M-A49-001-ASP), and the Center for Emergent Functional Matter Science of National Yang-Ming Chiao-Tung University (NYCU) from the Featured Areas Research Center Program within the framework of the Higher Education Sprout Project by the Ministry of Education (MOE) in Taiwan. M.-C. Chen also

gratefully acknowledges the funding provided by the NCU-Covestro Research Center.

References

1 H. Dixit, D. Punetha and S. K. Pandey, *Optik*, 2019, **179**, 969–976.
2 X. Jiang, Z. Zang, Y. Zhou, H. Li, Q. Wei and Z. Ning, *Acc. Mater. Res.*, 2021, **2**, 210–219.
3 X. Jiang, H. Li, Q. Zhou, Q. Wei, M. Wei, L. Jiang, Z. Wang, Z. Peng, F. Wang, Z. Zang, K. Xu, Y. Hou, S. Teale, W. Zhou, R. Si, X. Gao, E. H. Sargent and Z. Ning, *J. Am. Chem. Soc.*, 2021, **143**, 10970.
4 B. Bin Yu, Z. Chen, Y. Zhu, Y. Wang, B. Han, G. Chen, X. Zhang, Z. Du and Z. He, *Adv. Mater.*, 2021, **33**, 2102055.
5 N. K. Noel, S. D. Stranks, A. Abate, C. Wehrenfennig, S. Guarnera, A. A. Haghighirad, A. Sadhanala, G. E. Eperon, S. K. Pathak, M. B. Johnston, A. Petrozza, L. M. Herz and H. J. Snaith, *Energy Environ. Sci.*, 2014, **7**, 3061.
6 F. Hao, C. C. Stoumpos, D. H. Cao, R. P. H. Chang and M. G. Kanatzidis, *Nat. Photonics*, 2014, **8**, 489.
7 J. Zhou, M. Hao, Y. Zhang, X. Ma, J. Dong, F. Lu, J. Wang, N. Wang and Y. Zhou, *Matter*, 2022, **5**, 683.
8 Z. Song, A. Abate, S. C. Watthage, G. K. Liyanage, A. B. Phillips, U. Steiner, M. Graetzel and M. J. Heben, *Adv. Energy Mater.*, 2016, **6**, 1600846.
9 S. J. Lee, S. S. Shin, Y. C. Kim, D. Kim, T. K. Ahn, J. H. Noh, J. Seo and S. Il Seok, *J. Am. Chem. Soc.*, 2016, **138**, 3974–3977.
10 R. L. Milot, G. E. Eperon, T. Green, H. J. Snaith, M. B. Johnston and L. M. Herz, *J. Phys. Chem. Lett.*, 2016, **7**, 4178–4184.
11 C. Kuan, R. Balasaravanan, S. Hsu, J. Ni, Y. Tsai, Z. Zhang, M. Chen and E. W. Diau, *Adv. Mater.*, 2023, **35**, 2300681.
12 R. Balasaravanan, C. Kuan, S. Hsu, E. Chang, Y. Chen, Y. Tsai, M. Jhou, S. Yau, C. Liu, M. Chen and E. W. Diau, *Adv. Energy Mater.*, 2023, **13**, 2302047.
13 K. Almasabi, X. Zheng, B. Turedi, A. Y. Alsalloum, M. N. Lintangpradipto, J. Yin, L. Guti, K. Kotsovos, A. Jamal, I. Gereige, O. F. Mohammed and O. M. Bakr, *ACS Energy Lett.*, 2023, **8**, 950.
14 R. Azmi, W. T. Hadmojo, S. Sinaga, C. Lee and S. C. Yoon, *Adv. Energy Mater.*, 2018, **8**, 1701683.
15 A. Batdelger, S. Lee and S. Park, *ChemElectroChem*, 2023, **10**, e202300040.
16 S. Y. Kim, S. J. Cho, S. E. Byeon, X. He and H. J. Yoon, *Adv. Energy Mater.*, 2020, **10**, 2002606.
17 F. Ali, C. Roldán-Carmona, M. Sohail and M. K. Nazeeruddin, *Adv. Energy Mater.*, 2020, **10**, 2002989.
18 A. Magomedov, A. Al-ashouri, E. Kasparavic, S. Strazdaite, G. Niaura, M. Jošt, T. Malinauskas and S. Albrecht, *Adv. Energy Mater.*, 2018, **8**, 1801892.
19 M. Talaikis, G. Chistiakova, T. Bertram, A. Ma, C. J. Hages, R. Schlatmann, B. Rech and T. Malinauskas, *Energy Environ. Sci.*, 2019, **12**, 3356–3369.
20 E. Li, C. Liu, H. Lin, X. Xu, S. Liu, S. Zhang, M. Yu, X. Cao, Y. Wu and W. Zhu, *Adv. Funct. Mater.*, 2021, **31**, 2103847.
21 Z. Li, Q. Tan, G. Chen, H. Gao, J. Wang, X. Zhang, J. Xiu, W. Chen and Z. He, *Nanoscale*, 2023, **15**, 1676–1686.
22 A. Ullah, K. H. Park, H. D. Nguyen, Y. Siddique, S. F. A. Shah, H. Tran, S. Park, S. I. Lee, K. K. Lee, C. H. Han, K. Kim, S. J. Ahn, I. Jeong, Y. S. Park and S. Hong, *Adv. Energy Mater.*, 2022, **12**, 2103175.
23 W. Jiang, F. Li, M. Li, F. Qi, F. R. Lin and A. K. Jen, *Angew. Chem.*, 2022, **134**, 999077.
24 J. Wu, P. Yan, D. Yang, H. Guan, S. Yang and X. Cao, *Adv. Mater.*, 2024, **36**, 2401537.
25 S. Zhang, F. Ye, X. Wang, R. Chen, H. Zhang, L. Zhan, X. Jiang, Y. Li, X. Ji, S. Liu, M. Yu, F. Yu, Y. Zhang, R. Wu, Z. Liu, Z. Ning, D. Neher, L. Han, Y. Lin, H. Tian, W. Chen, M. Stolterfoht, L. Zhang, W. Zhu and Y. Wu, *Science*, 2023, **380**, 404–409.
26 D. Song, S. Narra, M. Y. Li, J. S. Lin and E. W. G. Diau, *ACS Energy Lett.*, 2021, **6**, 4179–4186.
27 A. Abid, P. Rajamanickam and E. W. Diau, *Chem. Eng. J.*, 2023, **477**, 146755.
28 E. W.-G. D. C. H. Kuan, S. N. Afraj, Y. L. Huang, A. Velusamy, C. L. Liu, T. Y. Su, X. Jiang, J. M. Lin and M. C. Chen, *Angew. Chem.*, 2024, **136**, e202407228.
29 S. N. Afraj, C. H. Kuan, J. S. Lin, J. S. Ni, A. Velusamy, M. C. Chen and E. W. G. Diau, *Adv. Funct. Mater.*, 2023, **33**, 2213939.
30 S. N. Afraj, C. Lin, A. Velusamy, C. Cho, H. Liu, J. Chen, G. Lee, J. Fu, J. Ni, S. Tung, S. Yau, C. Liu, M. Chen and A. Facchetti, *Adv. Funct. Mater.*, 2022, **32**, 2200880.
31 A. Velusamy, C. Yu, S. N. Afraj, C. Lin, W. Lo, C. Yeh, Y. Wu, H. Hsieh, J. Chen, G. Lee, S. Tung, C. Liu, M. Chen and A. Facchetti, *Adv. Sci.*, 2021, **8**, 2002930.
32 A. Velusamy and S. Yau, *J. Chinese Chem. Soc.*, 2023, **70**, 2046.
33 Z. Lan, J. Shao and Y.-W. Zhong, *Mol. Syst. Des. Eng.*, 2023, **8**, 1440–1455.
34 C. Kuan, Y. Ko and E. W. Diau, *ACS Energy Lett.*, 2023, **5**, 2423–2425.
35 E. Jokar, P. Y. Cheng, C. Y. Lin, S. Narra, S. Shahbazi and E. Wei-Guang Diau, *ACS Energy Lett.*, 2021, **6**, 485–492.
36 Y. Wang, S. Gu, G. Liu, L. Zhang, Z. Liu, R. Lin, K. Xiao, Z. Liu and H. Tan, *Sci. China Chem.*, 2021, **64**, 2025–2034.
37 Y. Xie, Q. Xue and H. Yip, *Adv. Energy Mater.*, 2021, **11**, 2100784.
38 L. Kong, Y. Luo, L. Turyanska, T. Zhang, Z. Zhang, G. Xing, Y. Yang, C. Zhang and X. Yang, *Adv. Funct. Mater.*, 2023, **33**, 2209186.
39 L. Liu, J. Lu, H. Wang, Z. Cui, G. Giorgi, Y. Bai and Q. Chen, *Mater. Reports Energy*, 2021, **1**, 100064.
40 E. Jokar, C. H. Chien, A. Fathi, M. Rameez, Y. H. Chang and E. W. G. Diau, *Energy Environ. Sci.*, 2018, **11**, 2353–2362.
41 L. Hao, M. Zhou, Y. Song, X. Ma, J. Wu, Q. Zhu, Z. Fu, Y. Liu, G. Hou and T. Li, *Sol. Energy*, 2021, **230**, 345–354.
42 T. S. Sherkar, C. Momblona, A. Jorge, M. Sessolo, H. J. Bolink and L. J. A. Koster, *ACS Energy Lett.*, 2017, **2**, 1214.
43 D. Song, L. Y. Hsu and E. W. G. Diau, *Mater. Adv.*, 2021, **2**, 754.
44 X. Liu, T. Wu, C. Zhang, Y. Zhang, H. Segawa and L. Han, *Adv. Funct. Mater.*, 2021, **31**, 2106560.

45 E. Jokar, C. H. Chien, C. M. Tsai, A. Fathi and E. W. G. Diau, *Adv. Mater.*, 2019, **31**, 1804835.
46 W. Liao, D. Zhao, Y. Yu, C. R. Grice, C. Wang, A. J. Cimaroli, P. Schulz, W. Meng, K. Zhu, R. Xiong and Y. Yan, *Adv. Mater.*, 2016, **28**, 9333.
47 J. Xi, Z. Wu, B. Jiao, H. Dong, C. Ran, C. Piao and T. Lei, *Adv. Mater.*, 2017, **29**, 1606964.
48 J. Liu, M. Ozaki, S. Yakumaru, T. Handa, R. Nishikubo, Y. Kanemitsu, A. Saeki, Y. Murata, R. Murdey and A. Wakamiya, *Angew. Chem.*, 2018, **57**, 13221–13225.
49 N. Ahn, K. Kwak, M. S. Jang, H. Yoon, B. Y. Lee, J. Lee, P. V Pikhitsa, J. Byun and M. Choi, *Nat. Commun.*, 2016, **7**, 13422.
50 G. Niu, W. Li, F. Meng, L. Wang, H. Dong and Y. Q, *J. Mater. Chem. A*, 2014, **2**, 705–710.
51 J. H. Noh, S. H. Im, J. H. Heo, T. N. Mandal and S. Il Seok, *Nano Lett.*, 2013, **13**, 1764–1769.
52 E. Nakanishi, R. Nishikubo, A. Wakamiya and A. Saeki, *J. Phys. Chem. Lett.*, 2020, **11**, 4043.
53 S. Shahbazi, M. Y. Li, A. Fathi and E. W. G. Diau, *ACS Energy Lett.*, 2020, **5**, 2508–2511.
54 W. Pervez and S. Ramsha, *J. Mater. Sci. Mater. Electron.*, 2020, **31**, 779–784.
55 E. J. Juarez-perez, M. Wu, F. Fabregat-santiago, K. Lakus-wollny, E. Mankel, T. Mayer, W. Jaegermann and I. Mora-sero, *J. Phys. Chem. Lett.*, 2014, **5**, 680.
56 Y. Ding, Y. Wu, Y. Tian, Y. Xu, M. Hou, B. Zhou, J. Luo, G. Hou, Y. Zhao and X. Zhang, *J. Energy Chem.*, 2021, **58**, 48.
57 P. Caprioglio, J. A. Márquez, A. Belen, M. Vilches, E. Kasparavicius, C. Gollwitzer, T. Malinauskas, M. Jo, L. Korte, A. Abate and B. Stannowski, *Science*, 2020, **370**, 1309.

